


High-Order Vector Bessel-Gauss Beams for Laser Micromachining of Transparent Materials

Justas Baltrukonis^{1,2,*}, Orestas Ulčinas,^{1,2} Sergej Orlov¹, and Vytautas Jukna^{1,3}

¹*Coherent Optics Laboratory, Center for Physical Sciences and Technology, Sauletekio Av. 3, Vilnius 10257, Lithuania*

²*Workshop of Photonics, Altechna R&D, Mokslininku St. 6A, Vilnius 08412, Lithuania*

³*Laser Research Center, Vilnius University, Sauletekio Av. 10, Vilnius 10223, Lithuania*

 (Received 28 December 2020; revised 15 July 2021; accepted 9 August 2021; published 1 September 2021)

Here, we present thorough research into high-order vector Bessel-Gauss beams from a theoretical perspective, with experimental realization and application to transparent-material laser micromachining. Efficient, stable, high-quality, and power-vector Bessel-Gauss beam generation using two geometric-phase-based optical elements, a high-order S -wave plate and an axicon in combination with simple optical elements, such as lenses, wave plates, and polarizers, is demonstrated. Ultrashort pulse-vector Bessel-Gauss beams are used to induce modifications in the glass, creating three-dimensional tubular structures of type I and type II modification in D263T glass. Furthermore, samples containing tubular modifications are tested for etch selectivity in the femtosecond-laser-induced chemical-etching method with KOH solution by etching throughout channels.

DOI: [10.1103/PhysRevApplied.16.034001](https://doi.org/10.1103/PhysRevApplied.16.034001)

I. INTRODUCTION

Microfabrication of transparent materials has been a fast-growing field of laser-matter interactions over the past decades. Typically employing short and high-power laser pulses, to cause nonlinear absorption inside a transparent material, this technique allows simple volume marking [1], multiphoton polymerization (MPP) [2], waveguide writing [3], volume nanograting formation [4], or selective chemical etching [5]. Improvements in laser-assisted manufacturing show no signs of stopping and follow simple tendencies to make processes faster, cheaper, and more accurate [6–8].

For many years, the microfabrication of transparent materials has relied on a focused Gaussian beam, giving a raster single-point modification process [9]. It is still the most versatile approach in many applications because the speed of beam positioning has been vastly improved (fast air-bearing stages, galvanometric and polygon scanners, etc.); however, this speed is reaching its limits because with increased speed the positioning accuracy deteriorates, in most cases. An improvement to increase the overall process speed is in beam-shaping technology, which can vary from a simple technique to a complicated one. For instance, beam-splitting technology, which gives multiple numbers of isolated and high-intensity peaks in both the X - Y [10,11] and X - Z planes [12], providing improvements,

from a few to hundreds of times, in industrial-process speeds. Likewise, the introduction of Bessel-Gauss beams [13] allows elongation of focal spots without deteriorating the spatial dimension to create an intense focal line [14,15]. These beams enable the single-pass cleaving of glass [16–18], an increase of the printing speeds of the MPP structure [19], the inscription of waveguides without the need to move the sample [20], or even the manufacture of high-aspect-ratio microchannels by adding a selective chemical-etching [21] step. Modification of the beam's transverse profile, creating, for example, a flat top [22] or even doughnut-shaped beams, is also done to enhance the ablation quality or to quickly ablate the desired shapes without moving the sample [23]. All abovementioned beam modifications show the versatility of laser microfabrication and demonstrate vast advantages in specific tasks, as they are purposely designed to improve speeds and optimize manufacturing costs.

The question arises whether it is possible to use beam-engineering techniques to create complex three-dimensional (3D) intensity distribution beams that can be used to manufacture 3D structures in transparent materials without moving the sample. The 3D beam-shaping techniques already lead to success when employing spatial light modulators (SLMs) [24]. Our previous works have also demonstrated complex beam-shaping techniques, allowing three-dimensional beam shaping with quasi-Bessel-Gauss beams employing SLMs [25–27], which allowed us to create controllable 3D laser-intensity

*justas.baltrukonis@ftmc.lt

distributions in air. However, the SLM diffraction efficiency and damage threshold are too low for microfabrication purposes, as high energies are needed to fabricate large three-dimensional structures, especially when the energy of the beam is distributed over a large volume. The beam-shaping technique that can enable the beam-intensity distribution to be changed with a high diffraction efficiency and with a high damage threshold is to use the geometrical phase in optical elements. The use of metasurface-based elements is promising [28], but, due to manufacturing difficulties, their quality quickly deteriorates when smaller and smaller elements are needed to fabricate incoming beam wavelengths in the optical or near-infrared regions, i.e., where most of the ultrashort-pulse laser central wavelengths and their harmonics are situated. For this reason, these elements work well for GHz and THz frequencies, as the elements are large enough that they can be fabricated without the need for expensive lithography techniques. On the other hand, volume nanogratings inscribed in fused silica [4] can be applied as the controllable geometric phase elements in the desired region. Femtosecond-laser-written volume nanogratings are well researched in the literature [29–31], but only recent advances in precise inscription processes and control of the fast-axis angle and retardance allow for commercially available high-efficiency nanograting-based optical elements to be used for beam shaping [32,33]. However, the resulting phase masks reported in previous publications [25–27] for the generation of an intricate 3D intensity distribution were too complex to write them as geometrical phase elements. To scale down the complexity of the problem, we use simpler vector Bessel beams (VBBs) for the microfabrication of transparent materials [34]. These beams are known for a tubular intensity distribution and complex and vector nature of polarization [35,36]. A setup for high-quality and high-power beam generation was proposed in Ref. [34] and involved a regular glass axicon and an S -wave plate. The axicon produces a Bessel-Gauss beam, while the S -wave plate spatially changes the beam polarization via inscribed spatially distributed nanogratings that act as localized polarization converters [37], as manufactured by the Workshop of Photonics (WOP). The resulting beam is exploited to create tubular modifications in glass, while separate polarization components are successfully used for glass-inscribing applications.

Continuing our work on VBBs and the exploitation of such beams for microfabrication purposes [33,38–40], we present a scheme for the generation of high-quality, high-power, and high-order VBBs and use them in the formation of tubular structures in transparent materials. We report on an experimental setup for high-power VBB generation employing a nanograting-based diffractive axicon and a high-order S -wave plate (both custom-made by WOP). Such beams are unique for their tubular intensity distribution, which is controlled by changing the order

of the VBB. They have even more complex polarization patterns than that of a first-order VBB; however, the updated optical setup allows even very-high-order VBBs to be achieved with very good efficiency and quality, with long-lasting and stable high-energy beam generation. The diameter of the tube increases almost linearly with increasing VBB order, n , while orthogonal polarization components consist of $2n$ intensity peaks positioned on the circle. Both the full beam and the individual linearly polarized constituents can be produced with the proposed optical setup and are employed to inscribe tubular modifications throughout D263T glass without moving the sample and/or laser beam. Thus, we demonstrate the fabrication of a 3D structure inside a transparent material employing only beam shaping. These structures can be used as waveguides for high-order Laguerre-Gaussian modes. A guiding mechanism can also be achieved in crystals where depressed cladding waveguides can be fabricated [41]. The higher-order VBBs may find application for wide-channel fabrication using the femtosecond-laser-induced chemical-etching (FLICE) method. As a proof of concept, our machined samples are further used for selective chemical-etching experiments in an attempt to create wide channels.

II. THEORETICAL BACKGROUND

We start here by introducing the concept of the geometrical phase (also known as the Pancharatnam-Berry phase) [33,42]. Let us assume that the optical element can be subdivided into pixels. The basic operation mode of those subpixels can be described using the formalism of the Jones matrix, M . Each subpixel has a spatially variant orientation of fast axis, usually described by the angle $\theta(x, y)$. Let us assume that a subpixel of such an element is a nanograting, which acts as a retarder to introduce a phase delay of kR . A geometrical phase element produced by this retardation is described as

$$T(x, y) = R^{-1}[\theta(x, y)]MR[\theta(x, y)] \\ = \begin{bmatrix} \cos^2\theta + e^{ikR}\sin^2\theta & (1 - e^{ikR})\cos\theta\sin\theta \\ (1 - e^{ikR})\cos\theta\sin\theta & e^{ikR}\cos^2\theta + \sin^2\theta \end{bmatrix}, \quad (1)$$

where $R(\theta) = \begin{bmatrix} \cos\theta & \sin\theta \\ -\sin\theta & \cos\theta \end{bmatrix}$ is the rotation matrix and $M = \begin{bmatrix} e^{i\phi_x} & 0 \\ 0 & e^{i\phi_y} \end{bmatrix}$ is the Jones matrix of a retarder, where ϕ_x and ϕ_y are the phase retardations of electric fields of perpendicular polarization components in the x and y directions, respectively, and represents the local behavior of nanogratings. Usually, retardation can be flexibly controlled in experiments and can be varied across the element; however, for simplicity and ease of use, we choose

for the retardance of the element to be constant and equal to half of the impingement on the element wavelength, $kR = \phi_y - \phi_x = \pi$, where k is the wave number; this gives us

$$T(x, y) = \begin{bmatrix} \cos 2\theta(x, y) & \sin 2\theta(x, y) \\ \sin 2\theta(x, y) & -\cos 2\theta(x, y) \end{bmatrix}. \quad (2)$$

Our main interest is in elements for which the local orientation of subpixels changes linearly with the azimuthal angle, φ , as $\theta(x, y) = q\varphi + \varphi_0$. This kind of behavior was observed in 2006 in the so-called q plates [43]. A q plate is a liquid-crystal (LC) device with an azimuthal pattern $[\theta(x, y)]$ of LC molecules around a central point. The geometrical pattern is characterized mainly by the topological charge, q , of the central singularity, which can be an integer or half an integer. Another common implementation is the so-called spatially variant half-wave plates (S -wave plates), which are produced by inducing local birefringence in glasses, and the geometrical phase is controlled by the orientation of the fast (slow) axis [37]. If $q = 1/2$, such an optical element converts a linearly polarized Gaussian beam into radially or azimuthally polarized beams [44]. Next, we have to constitute $\theta(x, y) = q\varphi$, which results in the expression for the Jones matrix, $T(x, y)$, of the S -wave plate. In a rather trivial fashion, we can demonstrate its action on the linearly polarized light, as follows:

$$\begin{aligned} E_{\text{rad}} &= \begin{pmatrix} \cos 2q\varphi & \sin 2q\varphi \\ \sin 2q\varphi & -\cos 2q\varphi \end{pmatrix} \begin{pmatrix} 1 \\ 0 \end{pmatrix} = \begin{pmatrix} \cos 2q\varphi \\ \sin 2q\varphi \end{pmatrix} \\ E_{\text{azi}} &= \begin{pmatrix} \cos 2q\varphi & \sin 2q\varphi \\ \sin 2q\varphi & -\cos 2q\varphi \end{pmatrix} \begin{pmatrix} 0 \\ 1 \end{pmatrix} = \begin{pmatrix} \sin 2q\varphi \\ -\cos 2q\varphi \end{pmatrix}. \end{aligned} \quad (3)$$

A Bessel vortex beam has a spatial amplitude distribution proportional to $J_m(\beta_0 r) \exp(im\varphi)$, where J_m is the m th-order Bessel function of the first kind, r is a radial coordinate, β_0 is a radial frequency [13], and m is the topological charge of the vortex. An unperturbed Bessel vortex does not diffract in the case of free propagation and is distinguished by the m th-order vortex core surrounded by decreasing intensity rings in the periphery that extends up to infinity. The experimentally realized spatially limited (apertured) Bessel vortices inherit invariable propagation only in a limited length called the Bessel zone [45,46]. The most commonly used method to experimentally generate a Bessel-Gauss beam is with the use of a glass cone named an axicon. This optical element adds a cone-shaped phase profile to the incoming beam, which, for the Laguerre-Gaussian (LG) $_{m0}$ beam, can be written as

$$E(r, \varphi) = a_0 e^{-r^2/d^2 - i\beta_0 r + im\varphi}, \quad (4)$$

where d is the beam radius; φ is an azimuth; and β_0 is a phase gradient determined by an axicon shape that can be

expressed as $\beta_0 \approx 2\pi(n_a - 1)\alpha/\lambda$, where λ is the wavelength, and n_a and α are the refraction index and wedge angle of the axicon, respectively. The maximum beam-intensity change with propagation distance has a distinct form proportional to $z \exp(-z^2)$ that has a steeper ascent than descent. The Bessel beam can also be visualized as an interference of plane waves, the wave vectors of which are placed on a cone; therefore, the spectrum of such beams is a ring. The apodized Bessel beam with a Gaussian, or in other words, the experimentally generated beam will have a ring structure in the far field; just the thickness of the ring will be proportional to the apodization function. For instance, the far field of the Bessel-Gauss vortex beam can be expressed as

$$S(\beta, \theta) = \pi d^2 I_m \left(\frac{\beta_0 \beta d^2}{2} \right) e^{-\frac{(\beta_0^2 + \beta^2)d^2}{4} + im(\theta_{\text{spe}} + \pi/2)}, \quad (5)$$

where I_m is the modified Bessel function of m th order, β is the spectral radius, and θ_{spe} is the spectral azimuth [46]. The far field of the Bessel-Gauss vortex beam has a Gaussian profile, which is located around the carrier frequency, $\beta_0 = k \sin \alpha_B$, where α_B is the angle of the Bessel beam. Let us now take a closer look at individual linearly polarized constituents of the vector beam after an optical element, see Eq. (3). The spatially variable half-wave plate modifies the far field [Eq. (5)] of the incident linearly polarized Bessel vortex, which is multiplied either by $\cos(2q\theta_{\text{spe}})$ or by $\sin(2q\theta_{\text{spe}})$. Let us assume that the incident polarization is oriented in the x direction, see Eq. (3). We recall Euler's formulas, $2 \cos(2q\theta_{\text{spe}}) = \exp(2iq\theta_{\text{spe}}) + \exp(-2iq\theta_{\text{spe}})$ and $2i \sin(2q\theta_{\text{spe}}) = \exp(2iq\theta_{\text{spe}}) - \exp(-2iq\theta_{\text{spe}})$. Therefore, the far field after the S plate can be written approximately [47] as

$$\begin{aligned} S(\beta, \theta) &\approx \left[I_{m+2q} \left(\frac{\beta_0 \beta d^2}{2} \right) e^{i(m+2q)(\theta_{\text{spe}} + \pi/2)} \right. \\ &\quad \left. \pm I_{m-2q} \left(\frac{\beta_0 \beta d^2}{2} \right) e^{i(m-2q)(\theta_{\text{spe}} + \pi/2)} \right] e^{-\frac{(\beta_0^2 + \beta^2)d^2}{4}}. \end{aligned} \quad (6)$$

Therefore, after the far field is transformed into the field, the linearly polarized constituents are superpositions of two Bessel vortices with topological charges $m + 2q$ and $m - 2q$:

$$E_{x,y}(r, \varphi) \approx \left[J_{m+2q}(\beta_0 r) e^{i(m+2q)\varphi} \pm J_{m-2q}(\beta_0 r) e^{i(m-2q)\varphi} \right] e^{-r^2/d^2}. \quad (7)$$

It is demonstrated that this superposition creates a rather rich and difficult structure [48,49]: for $m + 2q \geq |m - 2q|$

and $m - 2q \neq 0$, there exists a vortex with charge $m - 2q$ at the center of the beam at $\rho = 0$. Additionally, the cores of the single-charged vortices are situated at azimuthal angles $\varphi_k = \pi k / (4q)$, $k = 0, 1, 2, \dots, 4q - 1$ on the infinite number of circumferences. The presence of the minus sign rotates the pattern by $\pi / (4q)$. In our further development, we choose $m = 0$ (the incident beam has a Gaussian amplitude distribution) and $q = n/2$ is a half-integer number; here, $n = 1, 2, \dots$ is an integer. Thus, we can conclude that the linearly polarized E_x and E_y constituents are superpositions of two Bessel vortices with opposite charges, n and $-n$, and rotated by $\pi / (2n)$ with respect to each other. Numerically calculated transverse intensity distributions using Eq. (7) for the higher VBB and their individual polarization components are presented in Fig. 1. Three cases for the vector Bessel beam are chosen: $n = 1, 4$, and 6 . All mentioned properties are apparent in Fig. 1, such as central-ring expansion with an increase of the VBB order and the number of intensity peaks is double the VBB order. Yet another distinguishable and hardly measurable property of VBBs is the polarization pattern. Although all VBBs have a constant phase, the polarization vector rotates with the azimuth angle and the number of rotations is directly related to the order, n , of the beam. An example of such polarization patterns for a certain moment in time is depicted in Fig. 1 as gray arrows. The numerical simulation of the VBB generated via the axicon and higher-order S -wave plate propagation is also done.

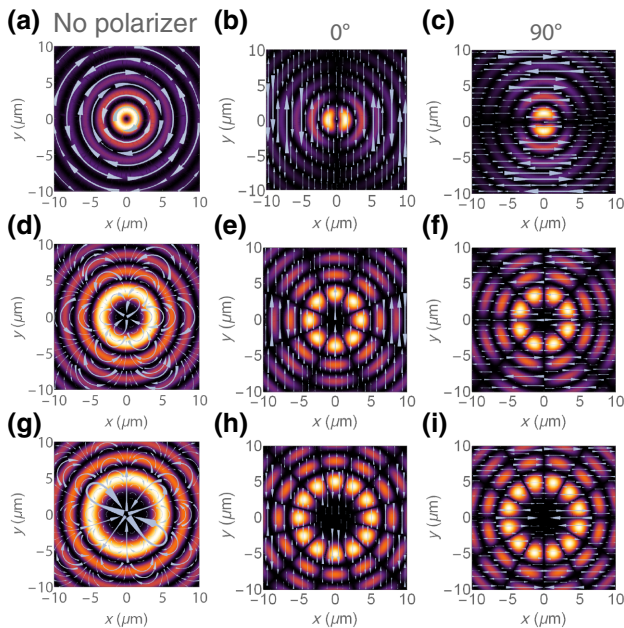


FIG. 1. Numerically calculated transverse intensity profiles of vector Bessel-Gauss beams of orders $n = 1$ (a), $n = 4$ (d), $n = 6$ (g), and their linearly polarized constituents (b), (c) for $n = 1$, (e), (f) for $n = 4$, and (h), (i) is for $n = 6$. Gray arrows depict stream lines of electric field.

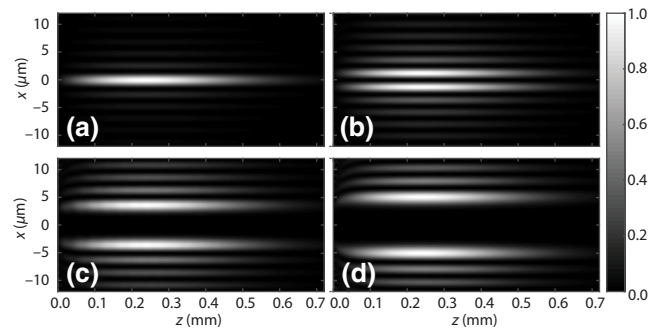


FIG. 2. Numerically calculated intensity profiles of $n = 0$ (a), $n = 1$ (b), $n = 4$ (c), $n = 6$ (d) VBBs in the X - Z plane. Scale as expected in ideal experimental setup.

Results for the intensity distributions in the Z - X plane over the propagation distance are shown in Fig. 2. As predicted, the simulation of Bessel-Gauss beams indicates a steeper ascent than descent of the axial intensity profile, while the length of the Bessel zone is closely connected to the initial beam width and the angle of the Bessel cone. All beam properties (beam size, wavelength, Bessel cone angle, etc.) used for the numerical simulation are as close as possible to the ideal case of our experimental setup.

III. EXPERIMENTAL SETUP

High-order VBBs are generated using a PHAROS (light conversion) Yb:KGW laser system, and micromachining experiments are performed with a FemtoLAB (WOP) microfabrication workstation. The fundamental Gaussian mode of the laser is directed through an axicon to transform it into a Bessel-Gauss beam. A high-order S plate is employed afterward for the generation of high-order VBBs (see Fig. 3). In our setup, both the axicon and n th-order S -wave plate are volume-nanograting-based diffractive elements and require a specific polarization to function. The

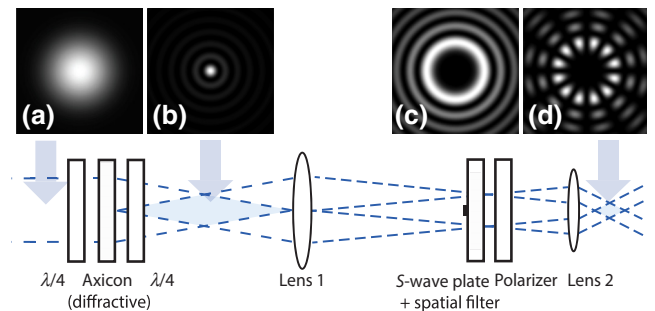


FIG. 3. Simplified experimental setup for the generation of a vector Bessel beam using a high-order S -wave plate. Lenses 1 and 2 represent here a $4f$ demagnifying imaging system. $\lambda/4$ denotes a quarter-wave plate. When present, the polarizer in the setup filters out individual linearly polarized constituents of the VBB.

diffractive element of the axicon changes the only phase of the beam. It is produced using a value of retardation of $kR = \pi$. To perform as intended, the polarization of the input beam has to be circular, as the value of retardation is kept constant at $kR = \pi$ over the full element area. For this reason, the diffractive optical element (DOE) axicon is placed between two $\lambda/4$ -wave plates, so the polarization of the beam is first converted from linear to circular, the beam interacts with the DOE, and the polarization is converted back to linear. Thus, a zero-order linearly polarized Bessel beam is generated, as required for the polarization conversion of the S plate to work as intended. The traditional refractive axicon made from transparent materials tends to have a rounded tip that greatly reduces the quality of the resulting beam and introduces a modulated axial intensity. In our previous work, we suggested using a spatial filter in the far field of the beam [34], i.e., a ring-shaped transmission mask, to remove unwanted far-field frequencies. This operation does improve the quality of the beam dramatically and allows us to generate quality first-order VBBs. However, the chrome ablated transmission ring (i.e., the spatial filter) degrades over time due to high fluence, which has to be filtered. Moreover, the spatial filter removes a substantial amount of energy from the beam (up to 30%), and therefore, the resulting efficiency is reduced. The setup is also sensitive and needs careful adjustment. The scheme proposed here, on the contrary, uses a geometric phase element (GPE) to act as an axicon. Thus, the beam quality is dramatically improved. The ability to precisely control the orientation of nanogratings inside a GPE enables us to generate a high-quality easily customizable DOE axicon [32], which is capable of high-quality Bessel-Gauss beam generation. As this GPE has a high damage threshold, the high quality of the generated beam remains, even for high-energy beams. In our particular case, we fabricate an axicon GPE to have a phase gradient, β_0 , of 95.82 rad/mm, which acts similarly to the ideal refractive axicon from fused silica with a wedge angle, α , of 2° for a wavelength of 1028 nm. Lens 1 in the setup in Fig. 3 is used to produce the far field of the Bessel beam. The S plate of order n is placed in the Fourier plane of lens 1. Different linearly polarized constituents are produced by placing a polarizer after the S plate. The second lens is used to construct a demagnified $4f$ telescope with a demagnification of 15.6 times. This setup allows the generation of a VBB with a cone angle of 14.06° in air. The diameter of the incident Gaussian beam is 4.5 mm at $1/e^2$ of the maximum beam intensity, which produces a Bessel zone with a length of about 0.35 mm, as measured at the FWHM.

We experimentally determine that placing an S -wave plate in the far field of the beam has many advantages. For example, the ring-shaped far field concentrates the beam energy further away from the center of the optical axis compared with the initial Gaussian beam, the energy

of which is continuously distributed, starting from the center to the sides, and its diameter is smaller than the radius of the Bessel beam's far-field radius. As the speed of polarization rotation is inversely proportional to the squared distance, a small deviation of placing an S -wave plate not exactly at the center of the Bessel beam's far field does not impact so much on the generated beam quality compared with the Gaussian-beam case. The second advantage is the fabrication speed of the element. The surface area of the Bessel-Gauss beam's far field is much smaller than that of the initial Gaussian beam; therefore, placing the GPE at the Bessel beam's far field eliminates the need to produce large-surface-area diffractive elements and saves time required for the fabrication of the element. The center of an S -wave plate, where high precision is required due to a rapid change of the fast axis and the possible occurrence of various fabrication defects, is not fabricated. Lastly, the nonfabricated center of the S -wave plate can be used to block the remaining zero-order diffraction, which comes from the GPE of the axicon. This arrangement of optical elements enables us to generate a high-quality Bessel-Gauss beam with an overall efficiency of 72%. The vast majority of energy loss arises from reflections of the uncoated optical elements, so the efficiency can be further improved. The nondiffracted part of the Gaussian beam, after it passes the diffractive axicon, has only

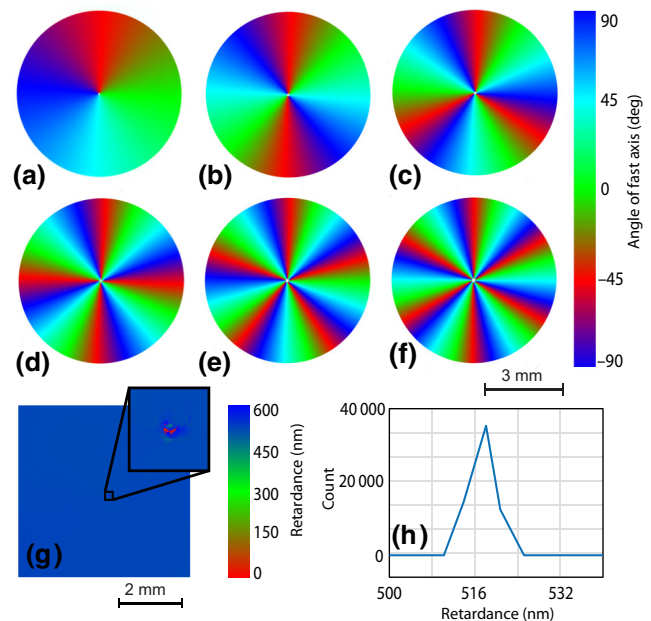


FIG. 4. Spatial distributions of the fast axes of different orders of S -wave plates. S -Wave plate orders are from $n = 1$ (a) to $n = 6$ (f). Retardance measurements with enlarged central part of the element (g) and a statistical plot of retardance (h). Measurements of fast-axis orientation and retardance are done with a Hinds Instruments Exicor MicroImager.

about 15% of the total energy. For comparison, the overall efficiency in a similar setup using a glass axicon and a special spatial filter with a few uncoated elements has an efficiency of about 60% [34].

Spatial distributions of the fast axes of the S -wave plates with orders from one to six are depicted in Fig. 4. Retardation is equal to $\lambda/2$ in the area of the element, and small variations of up to $\pm 2.5\%$, due to the manufacturing process, are observed. The orientation of the nanograting and the angle of the fast axis depend on the azimuth angle; gratings are rotated by πn over one full rotation, see Eq. (3). This approach to the GPEs results in a superb resistance to mechanical and environmental damage. All GPEs are tested for the laser induced damage threshold, and small differences in comparison to bare fused silica [50] are observed. For this reason, we can conclude that both elements under discussion (nanograting-based diffractive axicons and high-order S -wave plates) are great candidates for reliable use in high-energy applications.

IV. RESULTS

A. High-order VBB generation and characterization

For the successful application of structured light in microfabrication, high beam quality at high energies is essential. We analyze the performance of the setup depicted in Fig. 3 with the help of a CCD camera with a $60\times$ magnifying objective, and the results are depicted in Figs. 5 and 6. The free-space propagation of the beam

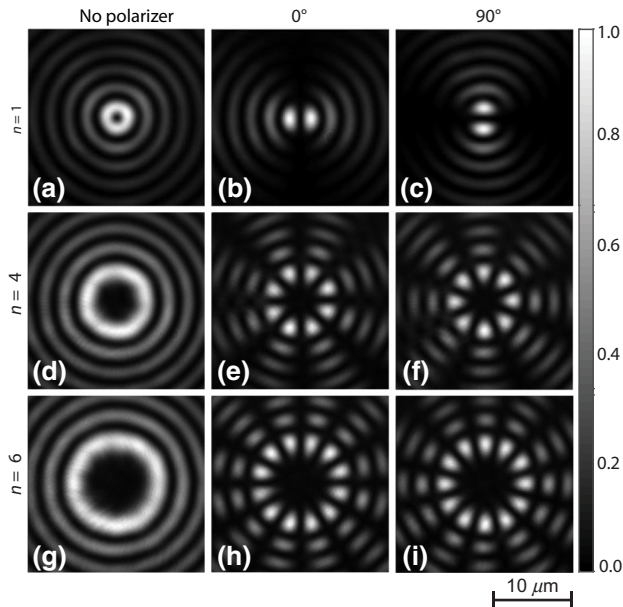


FIG. 5. Transverse intensity profiles of experimentally generated vector Bessel-Gauss beams of orders $n = 1$ (a), $n = 4$ (d), $n = 6$ (g), and their linearly polarized constituents (b),(c),(e),(f),(h),(i).

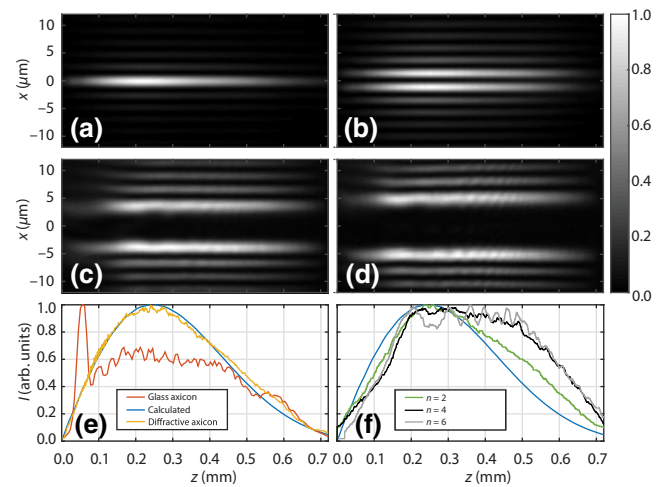


FIG. 6. Intensity profiles of the experimentally obtained beam in the X - Z plane. Orders of experimentally generated vector Bessel-Gauss beams are $n = 0$ (a), $n = 1$ (b), $n = 4$ (c), and $n = 6$ (d). Axial intensity distributions of typical refractive axicon, numerical simulation, and diffractive axicon (e); and axial intensity distributions of $n = 1$, $n = 4$, and $n = 6$ vector Bessel-Gauss beams (f).

is studied by translation of the imaging system along the z axis at a step size of $5 \mu\text{m}$. The intensity profiles of the first-, fourth-, and sixth-order VBBs are depicted in Figs. 5(a), 5(d), and 5(g), respectively. The intensity distributions of two orthogonally polarized constituents of the VBB are depicted in the second and third columns of Figs. 5. All profile measurements are performed at the center of the Bessel zone. The transverse intensity profiles of vector Bessel-Gauss beams are easily distinguished by the characteristic ring-shaped central part. The increase in the order of the VBB consequently enlarges the central ring, and therefore, the intensity contrast between the first and second intensity rings is reduced. The intensity distribution of linearly polarized constituents consists of $2n$ intensity peaks distributed on a circle. When the polarizer is rotated by $\pi/2$, the intensity distribution rotates by $\pi/2n$, and therefore, locations of the peaks on a ring can be adjusted quite easily.

The rotation of the polarizer does not change the detected power, which is half that of the initial power of the VBB. Theoretical analysis reveals that the intensity of the VBB has radial symmetry and that every ring contains the same amount of power, see the Bessel functions in Eq. (7). It also shows that, for the linearly polarized constituents, the intensity distribution has an azimuthal modulation; the ring is now modulated by $2n$ peaks and every peak on the ring has the same peak intensity (see Fig. 1). Experimentally generated VBB intensity profiles have a very close resemblance to the theoretically predicted distributions. The central ring has a small intensity modulation and the

modulation amplitude increases with the VBB order, but it does not exceed about 20%, and the main structure of the beam is maintained throughout the whole Bessel zone. Intensity profiles of linearly polarized constituents (i.e., beams after a polarizer) demonstrate peaks of high contrast. The intensity and shape of individual peaks are similar and close to those that are ideal. We suppose that irregularities may be caused by the nonideal laser beam, diffractive optical elements, and alignment issues, but overall the beam profile is very close to analytical expectations.

The theoretically predicted VBB should also sustain its symmetry over the full length of the Bessel zone. For this reason, we experimentally investigate the propagation of the VBB, and the experimentally measured intensity distributions in the X - Z plane are depicted in Fig. 6. The zeroth-order Bessel beam is generated without an S -wave plate and propagates similarly to a theoretically predicted Bessel-Gauss beam, see Fig. 6(a). It is used as a reference for further comparisons with situations when the S -wave plate is present in the setup. As expected, the appearance of an S -wave plate does not change the length of the Bessel zone. We do observe an expected increase of the diameter of the first intensity ring as the order of the VBB increases. In the cross section in the X - Z plane, this can be observed as the increased separation of two parallel tracks. Results depicted in Figs. 5 and 6 provide evidence of high-quality VBB generation. Indeed, no excessive axial intensity modulation or other irregularities are observed for the zeroth-order and $n = 1$ beams, see [Figs. 6(a) and 6(b)]. However, a slightly visible axial modulation does appear for $n = 4$ [Fig. 6(c)] and $n = 6$ [Fig. 6(d)]. The analytical maximum-intensity dependence on propagation distance comparisons with experimentally retrieved values are presented in Figs. 6(e) and 6(f). A comparison of the Bessel beam's axial intensity variation when generated with a GPE and typical glass axicon is depicted in Fig. 6(e). The blunt glass tip generates a large intensity modulation and a distinct intense initial peak, while the GPE-generated Bessel beam's intensity closely follows the analytical results. Fig. 6(f) shows the maximum-axial-intensity dependence on the propagation distance of higher-order VBBs for the X - Z planes depicted in Figs. 6(b)–6(d). Small irregularities might appear for higher-order n beams. This is naturally caused by the complexity of polarization patterns and intensity distributions, so the VBB becomes more sensitive. Despite the appearance of these artifacts, the nondiffracting nature of the beam is preserved, i.e., the central ring remains a ring from the start of the Bessel zone to the end of it. The contrast between adjacent rings is high, and therefore, a relatively good quality is achieved, which can be applied further for laser micromachining purposes.

B. VBB-induced modifications in glass

As we are satisfied with the quality of the experimentally observed VBBs, we move to applications. In this section, we show the exploitation of generated VBBs for the micromachining of glasses. The experimental scheme allows for the generation of high-power VBBs with the fluence of the beam high enough to exceed the damage threshold of transparent glasses. This investigation is important because high-order VBBs have a distinct 3D-shaped intensity distribution and, differently from the focused Gaussian beam, they should inscribe a similarly lengthy and complex structure without any movement of the sample or the beam. Of course, this is highly advantageous in terms of fabrication time and efficiency. While applications do vary from task to task, such flexibility in changes to the beam shape is highly desirable.

The goal of further experiments is to analyze the response of the glass to laser irradiation with VBBs. We are mainly interested in the type of modification, the shape induced by VBBs, and the evenness of inscribed modifications. We use common D263T borosilicate glass plates of 0.3-mm thick and analyze damage both on the surface and in the volume of samples. The induced surface and volume modifications are measured optically with an Olympus BX51 microscope (100 \times magnification of the objective). A few selected examples of a sample surface modified by a single-laser pulse are depicted in Figs. 7(a)–7(i). In a similar fashion, pictures depicting appropriate volume modifications are presented in Figs. 7(j)–7(r).

As expected, the ringlike intensity distribution of non-diffracting beams causes the appearance of ring-shaped surface damage. In this particular case, we produce damage throughout the sample with beams of 265.2 μ J in energy (half as much for linearly polarized constituents) and single pulses with a FWHM duration of 5 ps centered at a wavelength of 1028 nm. The surface modifications produced by a single-pulse VBB are depicted in Fig. 7; note that the first column is labeled “no polarizer.” We observe that higher-than-first-order VBBs ($n = 4$, $n = 6$) produce surface modifications that are ring shaped; however, the ringlike modification has irregularities over the circumference that are also noticeable in volume modifications. Apparently, the measured small beam-intensity modulations (observable in Fig. 5) are directly linked to irregularities in the ringlike structure of induced modifications. From the pictures of volume modification, we conclude that the tubular structure of modifications is sustained throughout the sample, given that the VBBs have enough power to propagate and modify the volume of the medium. On the contrary, surface damage produced by the linearly polarized constituents (see Fig. 7, second and third columns) is excellent, i.e., neat symmetrical surface damage is produced in a ring. The slight intensity variation of the peaks, which we discuss in the results A section, is not

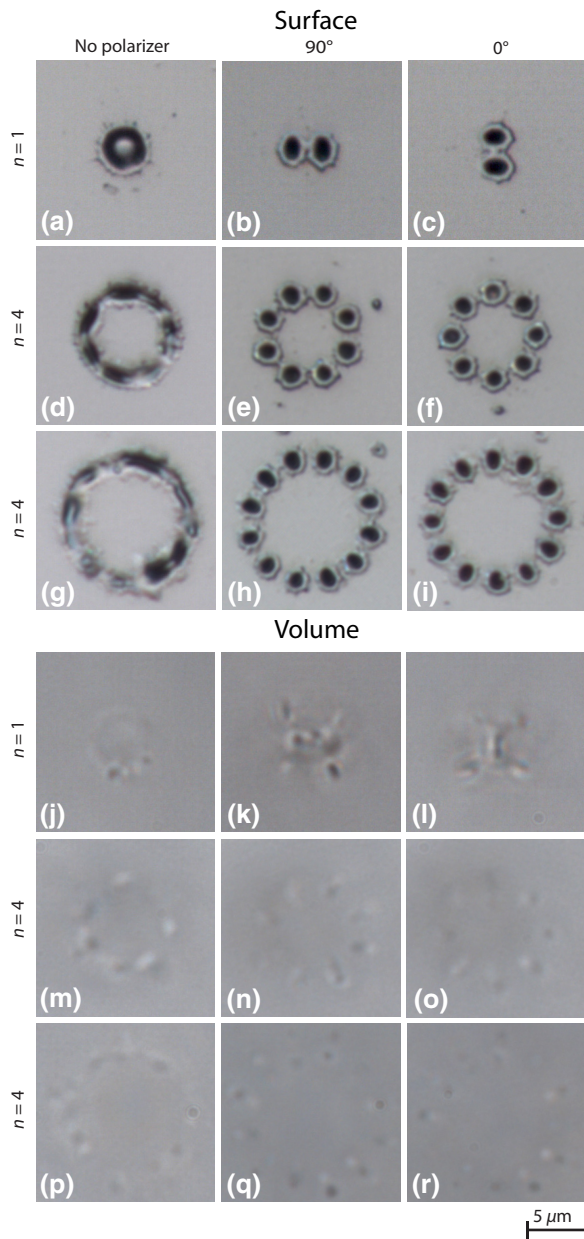


FIG. 7. Microscope images of voids formed on the surface of SCHOTT D263T glass (top images), and visible volume modifications in the sample (bottom images), produced by single-pulse vector Bessel-Gauss beams with orders of $n = 1$ (a),(j), $n = 4$ (d),(m), and $n = 6$ (g),(p). Modifications produced by linearly polarized x and y constituents of the VBBs are depicted in the second and third columns, respectively. Pulse duration 5 ps FWHM, pulse energy 265.2 μJ (a),(d),(g),(j),(m),(p) and 131.5 μJ (b),(c),(e),(f),(h),(i),(k),(l),(n),(o),(q),(r).

transferred noticeably to the surface modifications in this case. An exceptional crack formation, resembling the letter H is visible for the case of $n = 1$ [Figs. 7(k) and 7(l)] and resembles results reported previously in Ref. [34]. Linearly polarized constituents of high-order VBBs ($n = 4$, $n = 6$) cause starlike volume modifications to appear, i.e.,

slim cracks radiating from the center of the beam; however, they are localized at peaks of high intensity.

The Bessel zone length of VBBs (0.35 mm FWHM in air) is bigger than the sample thickness (0.3 mm; the refractive index is about 1.5). The axial beam intensity is not constant in the Bessel zone; therefore, fine adjustments are important, as changes in the sample position with respect to the axial intensity peak of the beam will change the beam intensity on the front and back surfaces of the material. This is especially crucial when uniform glass modification throughout the sample is desired. To overcome this, we increase the Bessel beam zone to be much larger than the thickness of the sample. We increase the beam diameter of the input Gaussian beam from 4.5 to 9 mm at $1/e^2$, which results in a 2 times increase in the length of the Bessel zone. The sample is centered over the Bessel zone. We test a wide range of parameters related to a laser micromachining scenario, to improve the evenness of the produced structures. Additionally, we investigate a multi-shot approach, when material damage is accumulated over multiple laser pulses. The contrast between the intensities in the first and second rings of the beam gets smaller as the order of the VBB increases. For the case of the sixth-order beam, it is equal to 1:0.49 (compared with 1:0.19 for a zeroth-order Bessel-Gauss beam). This naturally causes a smaller window of laser parameters for laser micromachining applications where only the first ring should modify the glass.

A small part of the experiments we perform is presented in Fig. 8. Here, we consider only a VBB of order $n = 6$ [Figs. 8(a) and 8(b)] and its linearly polarized constituents [Figs. 8(c) and 8(d)]. The accumulation of 500 000 shots with 1 ps FWHM pulses at a laser repetition rate of 40 kHz is used to generate these tracks. We choose to show the material modification of two pulse energies, 105 and 71.4 μJ . The first energy of 105 μJ is chosen because, with this energy, the first intensity ring would have enough intensity to induce modification of the front and back surfaces of the sample with a single shot. The energy of 71.4 μJ is about 30% lower than the single-shot surface-modification threshold and does not produce damage with a single shot. Two different fabrication conditions are investigated. The pulse energies are 105 μJ [Fig. 8(a)] for the first and 71.4 μJ [Fig. 8(b)] for the second case. Energies are half those for the linearly polarized components in Figs. 8(c) and 8(d). We use the same microscope and record images of the top surface, the volume, and the side view of a side-polished sample. In the first case, the energy of a VBB is higher [Fig. 8(a)], and a large amount of material from the back and front surfaces are ablated. As the ablated area acts as a screen, consecutive pulses are blocked; consequently, the central part of the beam does not fully penetrate the volume and the track is not fully formed. However, due to self-healing of nondiffracting VBBs, the beam is restored as it propagates further

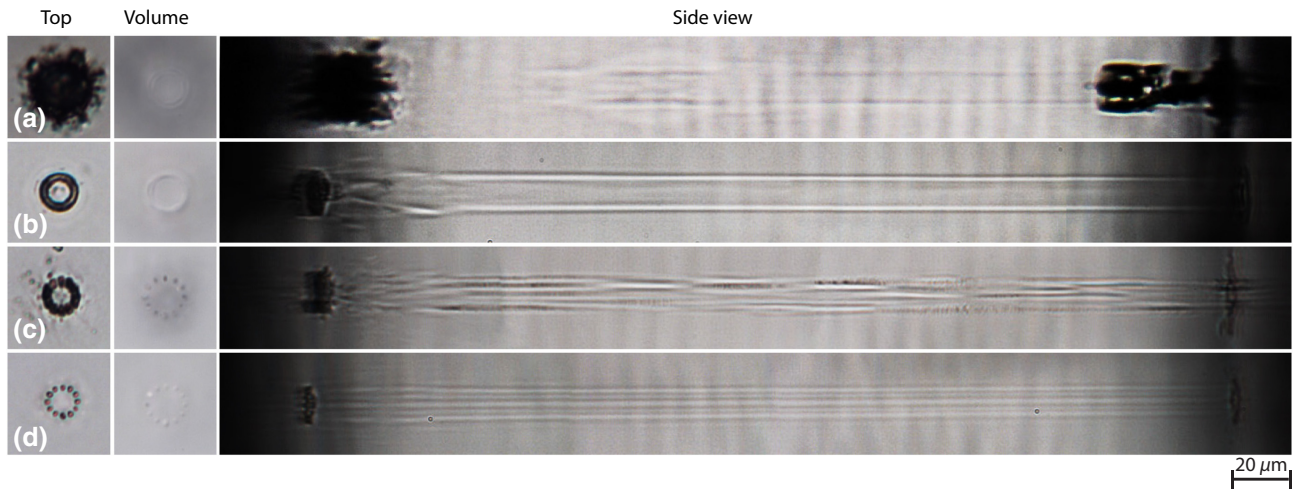


FIG. 8. Modifications in SCHOTT D263T glass sample with full $n = 6$ VBB (a),(b) and separate polarization components (c),(d). Pulse duration, 1 ps FWHM; number of pulses, 500 000; pulse energy, $105 \mu\text{J}$ (a) and $71.4 \mu\text{J}$ (b), and half that for separate components (c),(d). Microscope images show top, volume, and side views for each case.

from the shadow produced by the ablated surface. Due to the conical nature, energy flux from the periphery of the beam to the center of the beam enables self-healing and, as a result, partial volume modifications are still observed. In the second scenario, the energy of the pulses is lower; the results are presented in Fig. 8(b). A significantly lower amount of surface is ablated and, consequently, the beam is not screened. Hence, even refractive-index modification throughout the full sample with no apparent amplitude modification is successfully achieved. Modulations present in the transverse ring of the beam, see Figs. 7(g) and 7(p), are also significantly minimized due to damage-accumulation effects of the material.

Experiments are performed with linearly polarized constituents of the VBB in slightly different scenarios. We notice that ablation of the surface and beam shadowing are minimal in both low- and high-energy cases. However, we note darker tracks in the volume modification. This indicates that a type II modification is present, so cracks or nanovoids are formed. A natural cause of this can be found by looking at transverse intensity distributions. Separate intense peaks and lows on the ring induce local low- and high-material-stress areas, which are relaxed afterward through the formation of cracks. The second case (with a lower-energy beam) is also investigated [see Fig. 8(d)]. Modification induced in the material by a linearly polarized constituent of the VBB creates here very even tracks. Surface ablation is minimal; consequently, there is practically no modulation in the tubular structures. Furthermore, separate volumetric tracks can be easily distinguished from each other.

C. Selective chemical etching

Selective FLICE is a great tool to improve the microfabrication process by removing only laser-irradiated

material. The principle of FLICE is that the laser-irradiated area is etched up to a few hundred times faster [51], which allows the creation of complex hollow structures. Usually, a tightly focused Gaussian beam is used for FLICE for the most flexibility in producing desired shapes, 3D channels, and other structures [5]. However, when narrow and high-aspect-ratio channels are required, a Bessel-Gaussian beam shows a great promise because the fabrication time compared with that of a Gaussian beam is greatly improved [21,52].

Particular applications require spatially separated holes of larger diameter. This is a situation where material modifications induced by VBBs can be employed. As we demonstrate, VBBs have a controllable and much wider diameter of the central core than that of Bessel-Gauss beams and can be used for the fabrication of wide channels. The etching ratio of modified glass deeply depends on the type of modification [5]: when the refractive index changes, the etching rate increases slightly. However, when nanogratings and microcracks are formed, the etching rate increases significantly. The increase of the etching rate is related to a material change at the atomic level under laser irradiation [51]. Microcracks and nanogratings increase the etchant's capability to penetrate the modification and, as a result, speed up the chemical process. The ratio between the etching rates of modified and nonmodified glass is called selectivity, and this term will be further used in this work.

The FLICE method is widely used for various types of materials, with most uses related to fused silica [53,54]. Other applicable materials include YAG crystals [55], sapphire [56], or borosilicate glass [57]. In terms of etchants, there are two main options: low-concentration HF acid solution or less-toxic high-temperature KOH solution. The etching rate of HF is much higher than that

of KOH [53], but KOH features higher selectivity and is easier to work with. While conducting our experiments, we notice that higher selectivity is preferable; therefore, 30% 80 °C KOH solution is our choice for further experiments.

We perform additional experiments to examine various laser parameters and beam configurations. We select here a VBB with an order of $n = 6$ (Fig. 8). The diameter of the central core is about 10 μm . We investigate the effect of selective etching. A set of identical samples with laser-induced tubular modifications of the material are prepared for the chemical-etching experiment. Here, we change the pulse energy from 71.4 to 105 μJ in steps of 8.4 μJ (pulse energies, as usual, are twice as low for linearly polarized constituents) to study the dependence of etching selectivity on pulse energy. A separate sample is taken out of the KOH solution every 12 h; each side of a sample is polished and imaged. The resulting progress in etching over time is illustrated in Fig. 9, which presents the top surface of the sample (top image) and the side view of the sample (bottom image). The upper row shows results when a VBB beam is used [Fig. 9(a)–9(e)], and the results for the linearly polarized constituent are in the bottom row [Fig. 9(f)–9(j)].

We calculate the etching rate and selectivities. The values we obtain are averaged over 60 h, which is the time the whole experiment takes to complete. The etching rate of nonirradiated glass is 0.79 $\mu\text{m}/\text{h}$ and the sample thickness decreases by 95.3 μm at the end of the experiment.

We notice that the overall tendency is that the higher-energy beam generates material modifications that are etched faster. However, the shapes of the etched craters are different for the VBB and its linearly polarized constituents. A large amount of material is quickly etched in the first 24 h for the modified sample; consequently, the craters seen in Fig. 9(b) have the form of a broad U shape, starting from the bottom of the sample. The speed of etching in samples modified by high-energy beams progresses rapidly at the start and decreases dramatically after the first 12–24 h. We think that this is caused by excessive damage to the surface by the high-power beam and beam shadowing, as discussed earlier, see Fig. 8(a). Contrary to this, the etching speed for samples irradiated with beams of lower energy is almost constant at a rate of 1.67 $\mu\text{m}/\text{h}$. Samples are etched from both sides and the craters have a characteristic V shape. We obtain a value of selectivity, in this case, of 2.1. As we have mentioned previously, the VBBs with lower energy produce tubular structures and the change in refractive index is even throughout the sample [see Fig. 8(b)]. No significant beam shadowing is observed, which allows constant etching speeds to be achieved.

The selective etching of material modifications produced by the linearly polarized constituent is, in general, much faster and its selectivity is higher. This is observable in Figs. 9(f)–9(j), where the shape of the craters still resembles the V shape, and they are etched from both sides of the sample. Here, in all cases, steady etching over time can be

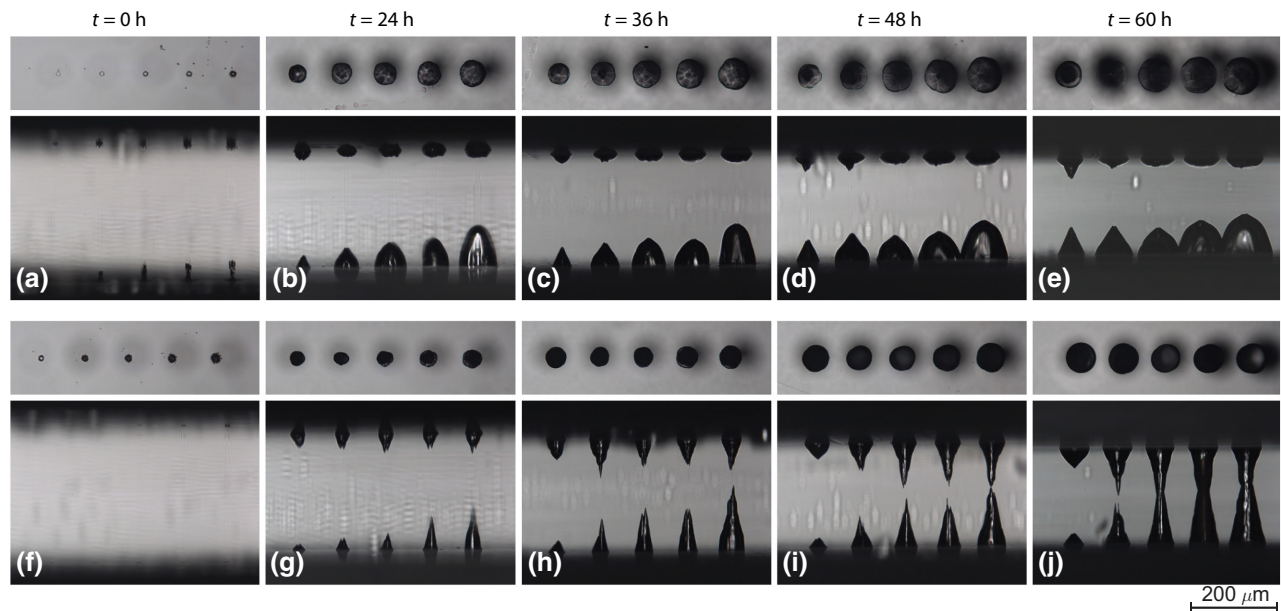


FIG. 9. Images of surfaces (top rows) and side views (bottom rows) of samples taken every 12 h after etching in 80 °C 30% KOH solution. Modifications in the volume are inscribed with a VBB beam with an order of $n = 6$ (a)–(e) and its linearly polarized constituents (f)–(j). In each picture, the pulse energy from left to the right changes from 71.4 to 105 μJ in 8.4 μJ intervals (energy is twice as low for the linearly polarized constituent). Pulse duration, 1 ps FWHM; number of pulses, 500 000, with 50 kHz repetition rate.

observed. The rate of etching increases with an increase in pulse energy and an even cone-shaped hole is etched. The maximum etching rate here is $3.23 \mu\text{m/h}$, and a selectivity of 4.07 is reached for the highest-pulse-energy value of $105 \mu\text{J}$. We conclude that a constant speed of etching can be achieved when the material is modified evenly. Another important factor here is the generation of a second type of modifications, see the darker trails in Fig. 8(d). The shapes of the holes now resemble an hourglass. The base diameter is $70 \mu\text{m}$ and the cone angle is from 9° to 12° . The multitrack nature of the linearly polarized constituent leaves a footprint on the final etched hole. The rates of etching are slightly higher on separate tracks and this causes the appearance of a rough surface of holes. Nevertheless, we report that the holes are fabricated consistently using a single linearly polarized constituent of the VBB. These results provide some insights into the dependence of etching rate on the type of modification and the use of VBBs and their linearly polarized constituents for glass modifications.

V. CONCLUSIONS

We propose an experimental setup for the generation of high-quality and high-energy VBBs. Quality is ensured by the elements produced by a technique involving volume nanogratings, which are sustainable due to the high input power. The design of such GPEs is successfully implemented. As our experimental verification demonstrates, both transverse and longitudinal planes of the VBBs and their linearly polarized constituents show no discrepancies with our theoretical expectations.

In our experiments, we use D263T borosilicate glass to modify its surface and volume with high-order VBBs and their constituents in both the single and multishot regimes. An inscription of smooth three-dimensional structures of refractive-index changes is possible when the energy of the VBBs (and their constituents) is lower. When the energy of the beam is too high, excessive surface ablation is observed, and the structure of volume modification is inhomogeneous due to shadowing. Interestingly, for linearly polarized constituents, these effects are less pronounced, as microcracks and microvoids with separate tracks are formed.

Lastly, we perform experiments using FLICE technology. Volume structures, which are laser micromachined, are systematically tested for the fabrication of voids throughout using selective chemical etching. We find that smooth and even changes in refractive index generated by a VBB are etched at lower rates. We achieve no etching of through holes. On the other hand, type II modifications are produced with higher-power linearly polarized constituents of VBBs, and this allows us to reach an etching rate of $3.23 \mu\text{m/h}$ and selectivity of 4.07. This is more than enough to create tapered holes in a 0.3-mm-thick D263T glass sample. Results from this study

provide useful information and will act as a guide for the laser community interested in the generation of high-quality and high-power VBBs and their application for laser microfabrication.

ACKNOWLEDGMENTS

This project has received funding from the European Social Fund (Project No. 09.3.3-LMT-K-712-01-0167) under a grant agreement with the Research Council of Lithuania (LMTLT).

-
- [1] R. D. Simmonds, P. S. Salter, A. Jesacher, and M. J. Booth, Three dimensional laser microfabrication in diamond using a dual adaptive optics system, *Opt. Express* **19**, 24122 (2011).
 - [2] S. Maruo and J. T. Fourkas, Recent progress in multiphoton microfabrication, *Laser Photonics Rev.* **2**, 100 (2008).
 - [3] S. Nolte, M. Will, J. Burghoff, and A. Tuennermann, Femtosecond waveguide writing: A new avenue to three-dimensional integrated optics, *Appl. Phys. A* **77**, 109 (2003).
 - [4] M. Beresna, M. Gecevičius, and P. G. Kazansky, Ultrafast laser direct writing and nanostructuring in transparent materials, *Adv. Opt. Photonics* **6**, 293 (2014).
 - [5] K. C. Vishnubhatla, N. Bellini, R. Ramponi, G. Cerullo, and R. Osellame, Shape control of microchannels fabricated in fused silica by femtosecond laser irradiation and chemical etching, *Opt. Express* **17**, 8685 (2009).
 - [6] H. Misawa and S. Juodkakis, *3D Laser Microfabrication: Principles and Applications* (John Wiley & Sons, Weinheim, 2006).
 - [7] R. Osellame, G. Cerullo, and R. Ramponi, *Femtosecond Laser Micromachining: Photonic and Microfluidic Devices in Transparent Materials* (Springer Science & Business Media, Heidelberg, 2012), Vol. 123.
 - [8] R. R. Gattass and E. Mazur, Femtosecond laser micromachining in transparent materials, *Nat. Photonics* **2**, 219 (2008).
 - [9] F. Sima, K. Sugioka, R. M. Vázquez, R. Osellame, L. Kelemen, and P. Ormos, Three-dimensional femtosecond laser processing for lab-on-a-chip applications, *Nanophotonics* **7**, 613 (2018).
 - [10] N. Matsumoto, S. Okazaki, Y. Fukushi, H. Takamoto, T. Inoue, and S. Terakawa, An adaptive approach for uniform scanning in multifocal multiphoton microscopy with a spatial light modulator, *Opt. Express* **22**, 633 (2014).
 - [11] E. T. Ritschdorff, R. Nielson, and J. B. Shear, Multi-focal multiphoton lithography, *Lab Chip* **12**, 867 (2012).
 - [12] M. Golub, L. Doskolovich, N. Kazanskiy, S. Kharitonov, and V. Soifer, Computer generated diffractive multi-focal lens, *J. Mod. Opt.* **39**, 1245 (1992).
 - [13] J. Durnin, Exact solutions for nondiffracting beams. I. the scalar theory, *JOSA A* **4**, 651 (1987).
 - [14] R. Stoian, M. K. Bhuyan, A. Rudenko, J.-P. Colombier, and G. Cheng, High-resolution material structuring using

- ultrafast laser non-diffractive beams, *Adv. Phys.:* **X 4**, 1659180 (2019).
- [15] M. Duocastella and C. B. Arnold, Bessel and annular beams for materials processing, *Laser Photonics Rev.* **6**, 607 (2012).
- [16] R. Meyer, M. Jacquot, R. Giust, J. Safioui, L. Rapp, L. Furfaro, P.-A. Lacourt, J. M. Dudley, and F. Courvoisier, Single-shot ultrafast laser processing of high-aspect-ratio nanochannels using elliptical bessel beams, *Opt. Lett.* **42**, 4307 (2017).
- [17] K. Mishchik, R. Beuton, O. D. Caulier, S. Skupin, B. Chimier, G. Duchateau, B. Chassagne, R. Kling, C. Höningner, and E. Mottay *et al.*, Improved laser glass cutting by spatio-temporal control of energy deposition using bursts of femtosecond pulses, *Opt. Express* **25**, 33271 (2017).
- [18] M. Bhuyan, O. Jedrkiewicz, V. Sabonis, M. Mikutis, S. Recchia, A. Aprea, M. Bollani, and P. Di Trapani, High-speed laser-assisted cutting of strong transparent materials using picosecond bessel beams, *Appl. Phys. A* **120**, 443 (2015).
- [19] L. Xiao-Fan, W. Richard, S. O'Brien, and C. Liang-Yao, Fabrication of 3D templates using a large depth of focus femtosecond laser, *Chinese Phys. Lett.* **26**, 094203 (2009).
- [20] F. Xin, M. Flammini, F. Di Mei, L. Falsi, D. Pierangeli, A. J. Agranat, and E. DelRe, Using Bessel Beams to Induce Optical Waveguides, *Phys. Rev. Appl.* **11**, 024011 (2019).
- [21] Z. Wang, L. Jiang, X. Li, A. Wang, Z. Yao, K. Zhang, and Y. Lu, High-throughput microchannel fabrication in fused silica by temporally shaped femtosecond laser bessel-beam-assisted chemical etching, *Opt. Lett.* **43**, 98 (2018).
- [22] S. Rung, J. Barth, and R. Hellmann, Characterization of laser beam shaping optics based on their ablation geometry of thin films, *Micromachines* **5**, 943 (2014).
- [23] B. Wetzel, C. Xie, P.-A. Lacourt, J. M. Dudley, and F. Courvoisier, Femtosecond laser fabrication of micro and nano-disks in single layer graphene using vortex bessel beams, *Appl. Phys. Lett.* **103**, 241111 (2013).
- [24] C. Chang, Y. Gao, J. Xia, S. Nie, and J. Ding, Shaping of optical vector beams in three dimensions, *Opt. Lett.* **42**, 3884 (2017).
- [25] S. Orlov, V. Vosylius, P. Gotovski, A. Grabusovas, J. Baltrukonis, and T. Gertus, Vector beams with parabolic and elliptic cross-sections for laser material processing applications, *J. Laser Micro Nanoeng.* **13**, 280 (2018).
- [26] S. Orlov, A. Juršėnas, J. Baltrukonis, and V. Jukna, Controllable spatial array of bessel-like beams with independent axial intensity distributions for laser microprocessing, *J. Laser Micro Nanoeng.* **13**, 324 (2018).
- [27] S. Orlov, A. Juršėnas, E. Nacius, and J. Baltrukonis, Controllable spatial array of optical needles with independent axial intensity distributions for laser microprocessing, *Procedia CIRP* **74**, 589 (2018).
- [28] A. Li, S. Singh, and D. Sievenpiper, Metasurfaces and their applications, *Nanophotonics* **7**, 989 (2018).
- [29] Y. Shimotsuma, P. G. Kazansky, J. Qiu, and K. Hirao, Self-Organized Nanogratings in Glass Irradiated by Ultrashort Light Pulses, *Phys. Rev. Lett.* **91**, 247405 (2003).
- [30] M. Beresna, M. Gecevičius, and P. G. Kazansky, Polarization sensitive elements fabricated by femtosecond laser nanostructuring of glass, *Opt. Mater. Express* **1**, 783 (2011).
- [31] S. Richter, M. Heinrich, S. Döring, A. Tünnermann, S. Nolte, and U. Peschel, Nanogratings in fused silica: Formation, control, and applications, *J. Laser Appl.* **24**, 042008 (2012).
- [32] V. Anand *et al.*, All femtosecond optical pump and X-ray probe: Holey-axicon for free electron lasers, *J. Phys.:* *Photonics* **3**, 024002 (2020).
- [33] P. Gotovski, P. Šlevas, E. Nacius, V. Jukna, S. Orlov, J. Baltrukonis, O. Ulčinas, and T. Gertus, in *Laser-based Micro-and Nanoprocessing XIV*, (International Society for Optics and Photonics, 2020), Vol. 11268, p. 112681Y.
- [34] J. Baltrukonis, O. Ulčinas, S. Orlov, and V. Jukna, Void and micro-crack generation in transparent materials with high-energy first-order vector bessel beam, *JOSA B* **37**, 2121 (2020).
- [35] A. Niv, G. Biener, V. Kleiner, and E. Hasman, Propagation-invariant vectorial bessel beams obtained by use of quantized pancharatanam-berry phase optical elements, *Opt. Lett.* **29**, 238 (2004).
- [36] A. Dudley, Y. Li, T. Mhlanga, M. Escuti, and A. Forbes, Generating and measuring nondiffracting vector bessel beams, *Opt. Lett.* **38**, 3429 (2013).
- [37] M. Beresna, M. Gecevičius, P. G. Kazansky, and T. Gertus, Radially polarized optical vortex converter created by femtosecond laser nanostructuring of glass, *Appl. Phys. Lett.* **98**, 201101 (2011).
- [38] P. Šlevas, S. Orlov, E. Nacius, O. Ulčinas, P. Gotovski, J. Baltrukonis, and V. Jukna, in *Laser Applications in Micro-electronic and Optoelectronic Manufacturing (LAMOM) XXV*, (International Society for Optics and Photonics, 2020), Vol. 11267, p. 112670B.
- [39] J. Baltrukonis, O. Ulčinas, P. Gotovski, S. Orlov, and V. Jukna, in *Laser-based Micro-and Nanoprocessing XIV*, (International Society for Optics and Photonics, 2020), Vol. 11268, p. 112681D.
- [40] E. Nacius, P. Gotovski, V. Jukna, O. Ulčinas, T. Gertus, and S. Orlov, in *Laser Resonators, Microresonators, and Beam Control XXII*, (International Society for Optics and Photonics, 2020), Vol. 11266, p. 112660Z.
- [41] F. Chen and J. R. V. de Aldana, in *Pacific Rim Laser Damage 2015: Optical Materials for High-Power Lasers*, (International Society for Optics and Photonics, 2015), Vol. 9532, p. 95320M.
- [42] F. S. Roux, Geometric phase lens, *JOSA A* **23**, 476 (2006).
- [43] A. Rubano, F. Cardano, B. Piccirillo, and L. Marrucci, Q-plate technology: A progress review, *JOSA B* **36**, D70 (2019).
- [44] T. Bauer, S. Orlov, U. Peschel, P. Banzer, and G. Leuchs, Nanointerferometric amplitude and phase reconstruction of tightly focused vector beams, *Nat. Photonics* **8**, 23 (2014).
- [45] F. Gori, G. Guattari, and C. Padovani, Bessel-gauss beams, *Opt. Commun.* **64**, 491 (1987).
- [46] V. Jarutis, R. Paškauskas, and A. Stabinis, Focusing of laguerre-gaussian beams by axicon, *Opt. Commun.* **184**, 105 (2000).
- [47] A. Stabinis, S. Orlov, and V. Jarutis, Interaction of bessel optical vortices in quadratic nonlinear medium, *Opt. Commun.* **197**, 419 (2001).

- [48] S. Orlov, K. Regelskis, V. Smilgevičius, and A. Stabinis, Propagation of bessel beams carrying optical vortices, *Opt. Commun.* **209**, 155 (2002).
- [49] S. Orlov and A. Stabinis, Propagation of superpositions of coaxial optical bessel beams carrying vortices, *J. Opt. A: Pure and Appl. Opt.* **6**, S259 (2004).
- [50] Laser-induced damage threshold (lidt) measurement report, <https://www.wophotonics.com/wp-content/uploads/2020/03/LIDT-result-fs-regime.pdf>, accessed: 2020-04-06.
- [51] A. Marcinkevičius, S. Juodkazis, M. Watanabe, M. Miwa, S. Matsuo, H. Misawa, and J. Nishii, Femtosecond laser-assisted three-dimensional microfabrication in silica, *Opt. Lett.* **26**, 277 (2001).
- [52] L. A. Hof and J. Abou Ziki, Micro-hole drilling on glass substrates—a review, *Micromachines* **8**, 53 (2017).
- [53] S. Kiyama, S. Matsuo, S. Hashimoto, and Y. Morihira, Examination of etching agent and etching mechanism on femtosecond laser microfabrication of channels inside vitreous silica substrates, *J. Phys. Chem. C* **113**, 11560 (2009).
- [54] J. Qi, Z. Wang, J. Xu, Z. Lin, X. Li, W. Chu, and Y. Cheng, Femtosecond laser induced selective etching in fused silica: Optimization of the inscription conditions with a high-repetition-rate laser source, *Opt. Express* **26**, 29669 (2018).
- [55] A. Ródenas, M. Gu, G. Corrielli, P. Paiè, S. John, A. K. Kar, and R. Osellame, Three-dimensional femtosecond laser nanolithography of crystals, *Nat. Photonics* **13**, 105 (2019).
- [56] S. Juodkazis, Y. Nishi, and H. Misawa, Femtosecond laser-assisted formation of channels in sapphire using koh solution, *Phys. Status Solidi (RRL)—Rapid Research Letters* **2**, 275 (2008).
- [57] A. Crespi, R. Osellame, and F. Bragheri, Femtosecond-laser-written optofluidics in alumino-borosilicate glass, *Opt. Mater.: X* **4**, 100042 (2019).